JGR Oceans

RESEARCH ARTICLE
10.1029/2020JC016091

Key Points:
- A mooring beneath 79 North ice tongue reveals ocean temperatures warmer than previously observed
- Fjord circulation is consistent with glacial melt-driven overturning enhanced seasonally by runoff
- Rapid exchange with the shelf suggests that ocean variability strongly influences ice tongue melt

Correspondence to:
M. R. Lindeman,
mrlindem@ucsd.edu

Citation:
Lindeman, M. R., Straneo, F., Wilson, N. J., Toole, J. M., Krishfield, R. A., Beaird, N. L., et al. (2020). Ocean circulation and variability beneath Nioghalvfjerdsbræ (79 North Glacier) ice tongue. *Journal of Geophysical Research: Oceans*, *125*, e2020JC016091. https://doi.org/10.1029/2020JC016091

Received 16 JAN 2020
Accepted 5 AUG 2020
Accepted article online 10 AUG 2020

Ocean Circulation and Variability Beneath Nioghalvfjerdsbræ (79 North Glacier) Ice Tongue

Margaret R. Lindeman[1], Fiammetta Straneo[1], Nat J. Wilson[2], John M. Toole[2], Richard A. Krishfield[2], Nicholas L. Beaird[3], Torsten Kanzow[4,5], and Janin Schaffer[4]

[1]Scripps Institution of Oceanography, University of California, San Diego, CA, USA, [2]Woods Hole Oceanographic Institution, Woods Hole, MA, USA, [3]Department of Marine and Coastal Sciences, Rutgers University, New Brunswick, NJ, USA, [4]Alfred-Wegener-Institut Helmholtz-Zentrum flür Polar- und Meeresforschung, Bremerhaven, Germany, [5]Department of Physics and Mechanical Engineering, University of Bremen, Bremen, Germany

Abstract The floating ice tongue of 79 North Glacier, a major outlet glacier of the Northeast Greenland Ice Stream, has thinned by 30% since 1999. Earlier studies have indicated that long-term warming of Atlantic Intermediate Water (AIW) is likely driving increased basal melt, causing the observed thinning. Still, limited ocean measurements in 79 North Fjord beneath the ice tongue have made it difficult to test this hypothesis. Here we use data from an Ice Tethered Mooring (ITM) deployed in a rift in the ice tongue from August 2016 to July 2017 to show that the subannual AIW temperature variability is smaller than the observed interannual variability, supporting the conclusion that AIW has warmed over the period of ice tongue thinning. In July 2017, the AIW at 500 m depth in the ice tongue cavity reached a maximum recorded temperature of 1.5°C. Velocity measurements reveal weak tides and a mean overturning circulation, which is likely seasonally enhanced by subglacial runoff discharged at the grounding line. Deep inflow of AIW and shallow export of melt-modified water persist throughout the record, indicating year-round basal melting of the ice tongue. Comparison with a mooring outside of the cavity suggests a rapid exchange between the cavity and continental shelf. Warming observed during 2016–2017 is estimated to drive a 33 ± 20% increase in basal melt rate near the ice tongue terminus and a 14 ± 2% increase near the grounding line if sustained.

Plain Language Summary The 79 North Glacier in northeastern Greenland has a floating ice tongue that extends 70 km into 79 North Fjord. The floating ice has thinned by 30% since 1999, likely due to warming of the ocean underneath. To evaluate the role of the ocean in driving this change, we deployed sensors that measured ocean temperature, salinity, and currents in the fjord under the ice for 9 months between August 2016 and July 2017. We find that the ocean was warmer during this period than in earlier observations and that the change over this period was small compared to changes between years. We also find that warm, salty water flows into the deep part of the fjord year-round, driving melting of the ice tongue. This results in relatively cold and fresh waters being exported at shallower depths. By comparing these observations with a record from outside the fjord, we show that ocean changes on the continental shelf rapidly affect the ocean under the ice tongue. Finally, we observe similarly warm ocean temperatures in summer 2018, suggesting that warming observed in 2016–2017 was sustained for at least 1 year, likely driving continued thinning of the ice tongue.

1. Introduction

Ice tongues, floating extensions of glaciers, have historically been common features of many of Greenland's major outlet glaciers. However, several of these have broken apart over the past 20 years as ocean and air temperatures have warmed (Hill et al., 2018). Nioghalvfjerdsbræ (79 North Glacier: 79NG) terminates in a 70 km long ice tongue, currently the largest in Greenland (Wilson et al., 2017), which is confined within Nioghalvfjerdsfjorden (79 North Fjord; Figure 1a). The 79NG ice tongue thinned by 30% between 1999 and 2014, but its extent has not decreased significantly (Mouginot et al., 2015). In contrast, the ice tongue of nearby Zachariæ Isstrøm (ZI) lost 95% of its area during the same period (Mouginot et al., 2015). The thinning of 79NG and collapse of ZI, the two major outlets of the Northeast Greenland Ice Stream (NEGIS),

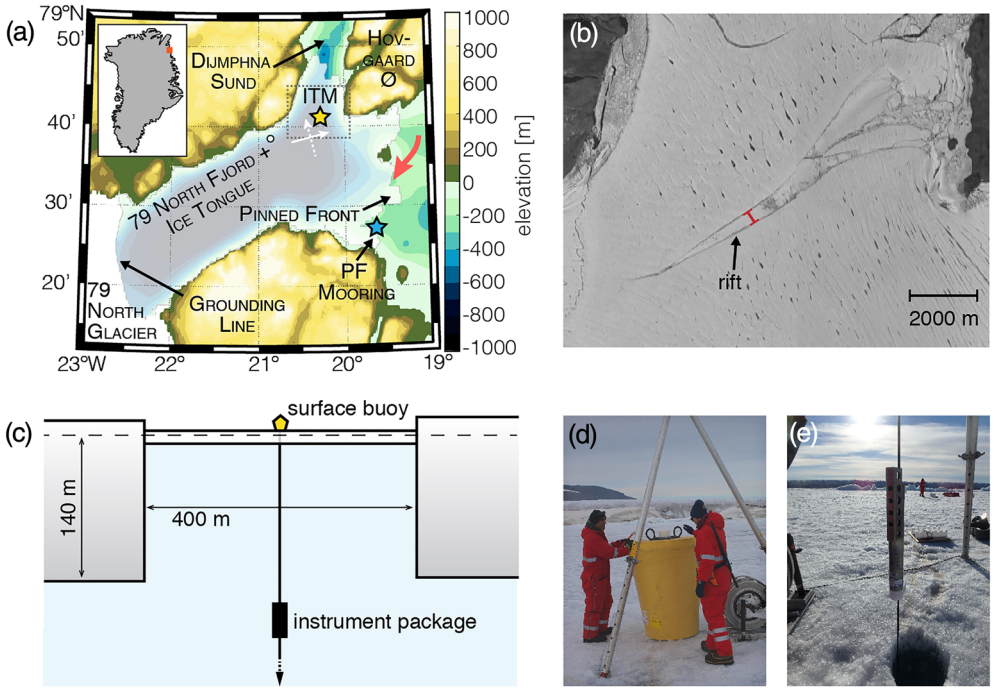

Figure 1. (a) Map of 79 North Fjord and ice tongue using BedMachine topography (Morlighem et al., 2017a, 2017b), including locations of the Ice Tethered Mooring (ITM; yellow star) and Pinned Front mooring (PF; blue star). White arrows show the inferred along-fjord (solid) and cross-fjord (dashed) axes at the ITM site (see section 3.2). The red arrow indicates the location of primary AIW inflow (Schaffer et al., 2020). The white circle indicates the location of the 1998 temperature profile shown in Figure 2a. Gray dotted box around ITM indicates location of satellite image in (b). Inset: Map of Greenland coastline with orange box indicating the location of 79 North Glacier and Fjord. (b) Satellite image of ice tongue rift (July 2013; image from Google & Maxar Technologies). The red line spanning the rift is 400 m long and indicates the approximate ITM location. (c) Schematic of ITM configuration (not to scale). The surface buoy sits on sea ice that formed where the ice tongue rifted apart. The draft of the ice tongue on either side of the rift is approximately 140 m, so the 150 m instrument is 10 m below the ice base. (d) ITM surface buoy at time of deployment. (e) Deployment of an ITM MicroCAT.

are thought to be driven by increased ocean melt driven by warming, as observed in the breakup of Sermeq Kujalleq ice tongue (also known as Jakobshavn Isbræ; Bjørk et al., 2015; Holland, Thomas, et al., 2008; Motyka et al., 2011; Mouginot et al., 2015). The loss of buttressing of upstream ice flow provided by the ZI and Sermeq Kujalleq ice tongues resulted in the retreat of their respective grounding lines along retrograde bed slopes and the acceleration of ice discharge (Joughin et al., 2014; Mouginot et al., 2015). The ocean's role in the evolution of 79NG ice tongue is therefore important to the future stability of NEGIS, which accounts for 12% of ice discharge from the Greenland Ice Sheet and holds a 1.1 m sea level equivalent (Dupont & Alley, 2005; Morlighem et al., 2014).

79NG Fjord is entirely covered by the ice tongue and is connected to the continental shelf ocean via Dijmphna Sund to the north and by several channels beneath the bathymetrically pinned ice front to the east (Figure 1a; Mayer et al., 2000). Previous studies of 79NG Fjord indicate that warm Atlantic Intermediate Water (AIW) present on the continental shelf flows into the ice tongue cavity through the eastern pinned front and drives significant melting of the ice tongue base, particularly in the vicinity of the grounding line (Schaffer et al., 2017, 2020; Wilson & Straneo, 2015; Wilson et al., 2017). The AIW is transformed through this process, becoming colder and fresher (and thus more buoyant) through the input of glacial meltwater. This glacial modification is thought to drive an estuarine-like circulation, with AIW flowing toward the grounding line at depth and shallow export of glacially modified water through both branches of the fjord (Schaffer et al., 2020; Wilson & Straneo, 2015).

The warm AIW present on the continental shelf is sourced from Atlantic waters transported northward in the West Spitsbergen Current (WSC) toward Fram Strait, the primary gateway for heat, freshwater, and sea ice exchange between the Arctic Ocean and Nordic Seas (de Steur et al., 2014; Marnela et al., 2013). About

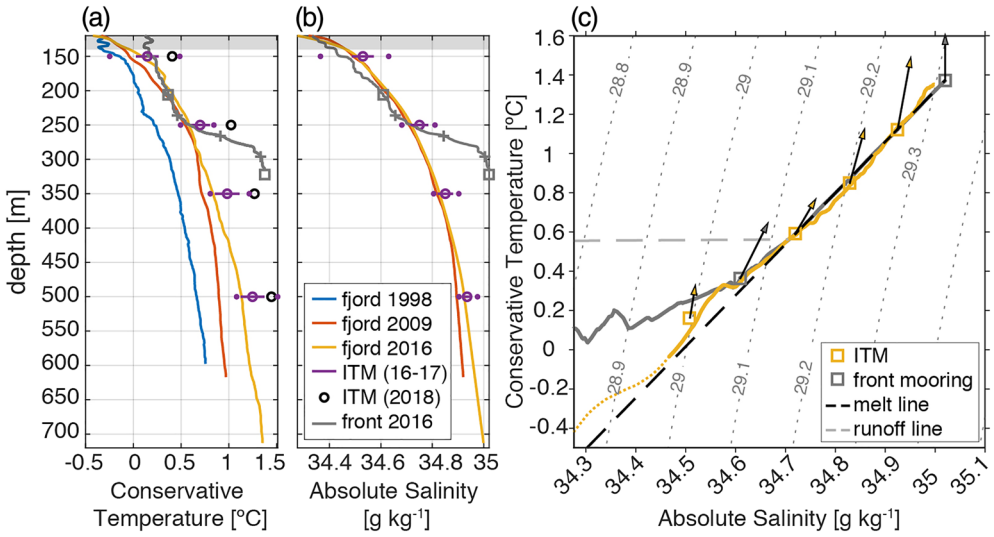

Figure 2. (a) Conservative Temperature and (b) Absolute Salinity profiles in the 79NG cavity from 1998 (blue; Schaffer & Mayer, 2018), 2009 (red; Straneo, 2020), and 2016 (yellow). The location of the 1998 profile is shown in Figure 1a; the 2009 and 2016 profiles are from the ice tongue rift. The time mean of the 2016–2017 time series of temperature and salinity at each ITM depth is plotted as an open circle (purple). One standard deviation is indicated by the purple line, with the record minimum and maximum indicated by purple dots. The average temperature at each depth during early summer 2018 is plotted as a black circle (see section 2). August 2016 Conservative Temperature and Absolute Salinity profiles from the Pinned Front (PF) mooring location are plotted as gray lines, with squares indicating the depths of moored CTDs and crosses indicating the depths of moored thermistors. Shading above 140 m indicates the approximate ice tongue draft near the ITM location. (c) Conservative Temperature and Absolute Salinity from the August 2016 profiles at the ITM (yellow) and PF (gray) locations in August 2016. The squares indicate the mean temperature and salinity observed by each Microcat over the first 24 hr of the mooring records. The dashed lines indicate the mixing lines associated with basal melt (black) and subglacial runoff (light gray). The arrows indicate the change in temperature and salinity properties at each moored instrument through the end of each mooring record (July 2017 at the ITM, September 2017 at PF).

half of WSC Atlantic water transport is recirculated in the 320 km wide Fram Strait and returns southward in the East Greenland Current (EGC) (de Steur et al., 2014; Hattermann et al., 2016; Marnela et al., 2013). Schaffer et al. (2017) suggest that Atlantic waters in the EGC may be transported onto the 300 km wide continental shelf via eddy- and tidally driven mixing. AIW is thus created through mixing of Atlantic waters with colder Polar Water (PW) of Arctic origin present at shallow depths on the shelf. They estimate a 1.5 year time scale for ocean property anomalies in the WSC to be advected to the 79NG terminus. The temperature of northbound Atlantic waters in the WSC increased by 0.06°C year^{-1} from 1997 to 2010, which has likely affected AIW properties on the shelf, but with a smaller magnitude due to modification by mixing (Beszczynska-Möller et al., 2012; Schaffer et al., 2017). Warming of deep AIW within 79NG cavity is inferred from three ocean temperature profiles in summers 1998, 2009, and 2014 (Figure 2a; Mayer et al., 2018; Wilson & Straneo, 2015), but it is unknown whether these observations accurately reflect a significant trend or are biased by subannual or interannual variability. Sustained warming of AIW reaching the 79NG ice tongue base would cause an increase in basal melt rate, but more measurements are needed to characterize the relationship between offshore ocean property changes, changes on the continental shelf, and their propagation into the 79NG cavity.

In addition to far-field ocean warming, atmospheric warming beginning around 2000 may have had significant impacts on variability in the 79NG cavity (Khan et al., 2014). Both air and ocean warming likely contributed to the breakup of the Norske Øer Ice Barrier (NØIB), a region of landfast sea ice on the continental shelf adjacent to 79NG and ZI, which was formerly quasipermanent but has broken up nearly every summer since 2001 (Sneed & Hamilton, 2016). In addition to the role of sea ice in modulating air-ocean exchanges, landfast sea ice can provide backstress on floating glacier fronts (Reeh et al., 2001), and the loss of the NØIB may have contributed to the destabilization of the ZI ice tongue (Khan et al., 2014). Furthermore, the northeastern sector of the Greenland Ice Sheet, which is drained primarily through 79NG and ZI, has seen a dramatic decrease in its surface mass balance since 2000, resulting in increasing runoff of ice

melt (MacFerrin et al., 2019; Mouginot et al., 2019). A fraction of the ice sheet surface melt drains to the bed through cracks in the ice and is routed to the margins through subglacial channels, entering the ocean at glacier grounding lines, where it drives enhanced basal melt by increasing turbulent heat transfer to the ice base as it rises buoyantly (Chu, 2014; Jenkins, 2011; Straneo & Cenedese, 2015). At 79NG, additional surface melt is likely exported through supraglacial rivers and enters the surface ocean at the ice tongue terminus, as has been observed at, for example, Petermann Gletscher in northern Greenland (Johnson et al., 2011) and Nansen Ice Shelf in Antarctica (Bell et al., 2017).

The sensitivity of ice tongue melt to external ocean variability depends on its timing and magnitude as well as the time scales and mechanisms of exchange between the cavity and shelf (e.g., Holland, 2017). A melt-driven overturning circulation alone would drive a relatively slow exchange with the shelf (Wilson & Straneo, 2015), but recent studies indicate that AIW inflow into the 79NG cavity is hydraulically controlled by a sill outside the pinned front (Schaffer et al., 2020; Zhao et al., 2019) and may be modulated by remotely forced topographic Rossby waves (Münchow et al., 2020). Studies of other Greenland fjords have shown that exchange is enhanced by energetic shelf-driven flows and discharge of summer surface melt at the grounding line, both of which can accelerate renewal of fjord waters (Jackson et al., 2014; Straneo et al., 2010; Washam et al., 2018). Tidal currents and eddies have also been found to significantly enhance basal melt of Antarctic ice shelves (Arzeno et al., 2014; Hattermann et al., 2012; Padman et al., 2018). Previous observations in the ice tongue cavity do not include ocean currents and provide snapshots only of summer conditions, so the key processes driving variability in the 79NG cavity properties and circulation, and by extension ice tongue melt, are unknown.

In this paper, we present the first moored record of temperature, salinity, and currents in the 79NG ice tongue cavity. We analyze variability of water masses and circulation in the cavity over the 9-month record, which spans from August 2016 to July 2017, compare this with time series of ocean- and glacier-driven variability to identify possible mechanisms, and discuss the implications for basal melting of the ice tongue. Our results suggest that external ocean forcing and glacier-driven processes both drive significant variability in ocean properties and circulation and thus ice tongue melt.

2. Data

An Ice Tethered Mooring (ITM) was deployed in the 79NG ice tongue rift near Hovgaard Ø during the PS100 expedition of the RV *Polarstern* in August 2016 (Figures 1a, 1d, and 1e; AWI, 2017; Toole et al., 2016). The rift forms where the ice tongue splits into two branches, exposing the ocean surface and allowing sea ice to form, and is approximately 400 m wide in the vicinity of the ITM (Figure 1b). The sea ice thickness is on the order of meters, while the glacial ice draft in this area is approximately 140 m (Wilson et al., 2017), and the bottom depth is approximately 720 m (Figure 1c; Wilson & Straneo, 2015). The ITM location is approximately 13 km north and 18 km west of the primary AIW inflow location (Figure 1a; Schaffer et al., 2020). The inductive mooring had Sea-Bird Electronics SBE37 MicroCAT Conductivity, Temperature, and Depth (CTD) instruments and Nortek Aquadopp current meters at 150, 250, 350, and 500 m, recording observations every 15 min. Two temperature and salinity profiles were also collected using Lockheed Martin XCTD-1s (eXpendable CTDs) at the time of deployment (Straneo & Wilson, 2020). All timeseries were low-pass filtered with a fourth-order 33-hr Butterworth filter, and temperature and salinity measurements are reported as Conservative Temperature and Absolute Salinity (McDougall & Barker, 2011), unless otherwise specified. Uncertainties for each sensor are listed in Table 1. The ITM surface buoy transmitted real-time data and GPS locations every 24 hr through July 2017, excluding a 2-month gap beginning in late winter, for a total of nearly 9 months of data. During this time, the buoy position moved 450 m to the northeast, indicating a mean local ice flow speed of 1.3 m day^{-1}.

We assume that the ocean properties and circulation observed by the ITM below the ice shelf rift are representative of conditions at similar depths under the ice shelf base nearby. This assumption is particularly uncertain at 150 m, where ocean conditions are most likely to be affected by their proximity to the rift. Simulations by Jordan et al. (2014) suggest that an ice shelf rift affects the ocean below it most strongly when upstream ocean temperatures are close to freezing and currents are strong. In contrast, we find that temperatures at the ITM at 150 m are consistently well above freezing (section 3.5), currents are relatively weak (section 3.2), and stratification in the rift is stable (Figure 2b), limiting the potential for vertical mixing.

Table 1
Sensor Uncertainties According to Manufacturer Specifications

	Temperature (°C)		Salinity (g kg^{-1})		Velocity (cm s^{-1})
Sensor	*Accuracy*	*Resolution*	*Accuracy*	*Resolution*	*Accuracy*
MicroCAT	0.002	0.0001	0.004	0.0001	—
Aquadopp	0.01	0.01	—	—	0.5–0.6[a]
XCTD	0.02	0.01	0.04	0.02	—

[a]For observed velocity range.

While some influence from the rift cannot be ruled out, these factors support our interpretation of ITM observations as representative of cavity properties beneath the proximal ice base.

The pressure recorded by all ITM CTDs indicated shoaling of 14 m over the course of the record. This change occurred in several distinct events throughout the record that were observed simultaneously over all depths, suggesting that the wire rope at the surface buoy end was trapped in sea ice and lifted, likely by mechanical ice ridging. Because temperature increases with depth in this setting, this upward displacement of the sensors would be expected to move them into water that is colder and fresher (Figures 2a and 2b). At the time of the 2016 XCTD profile, shoaling of 14 m would be associated with cooling of 0.20°C at 150 m, 0.04°C at 250 and 350 m, and 0.02°C at 500 m. At all depths, the temperature and salinity change induced by shoaling is much smaller in magnitude than the observed temperature variability (section 3.1), but the reported warming is likely underestimated as a result of the shoaling.

The sea ice ridging is also a likely driver of the gaps in the mooring record, as it could have caused the ground lead to lose contact with the seawater, resulting in a loss of electrical continuity in the inductive modem loop. When the MicroCAT data ceased transmission in February and July 2017, the Aquadopp current meters, which also have temperature recorders, continued to transmit data for a few days longer. Data transmission from the Aquadopps also resumed for between 4 days (350 m) and 2 weeks (150 m) in June–July 2018. At each depth, a constant offset between the Aquadopp and MicroCAT temperature sensors was calculated from the overlapping parts of the timeseries and used to correct the Aquadopp sensor temperatures, which have a lower accuracy and resolution (Table 1). The 2018 Conservative Temperature values shown in Figure 2a are calculated using the mean temperature from this period and the mean salinity from the 2016–2017 record at each depth.

We compare the variability observed by the ITM within the cavity with a mooring record on the continental shelf outside the pinned ice front (Pinned Front mooring; PF), south of the presumed AIW inflow pathway (Figure 1a Schaffer et al., 2019). Its location is approximately 35 km southeast of the ITM and has a bottom depth of 322 m. This mooring was also deployed by the Alfred-Wegener Institute during the PS100 expedition in August 2016 and recovered in September 2017. The mooring was instrumented with temperature loggers at five depths between 206 and 322 m, with conductivity measurements at the shallowest and deepest instruments. For the instruments with no conductivity sensors, Conservative Temperature was calculated using the Absolute Salinity at the corresponding depth from the CTD profile at the time of deployment (Figure 2b; gray crosses). An upward-looking 150 kHz ACDP (TRDI Workhorse Quartermaster) measured velocity at 4 m vertical resolution between 38 and 314 m. Like the ITM timeseries, all PF timeseries were low-pass filtered with a fourth-order 33-hr Butterworth filter. Mayer et al. (2000) found that the ice tongue draft at the terminus near PF was approximately 100 m, though the southern portion of the terminus has retreated by about 10 km due to calving since that survey (Khan et al., 2014).

Ice sheet surface melt calculated by the Regional Atmospheric Climate Model (RACMO; Noël et al., 2018) over the 79NG Glacier catchment area defined by Slater et al. (2019) is used to estimate subglacial runoff, that is, surface melt that is discharged to the ocean through subglacial channels at the grounding line. The total volume of surface melt is an upper bound on subglacial runoff, because we expect that some of the melt is exported by supraglacial rivers or stored (e.g., in melt ponds on the ice tongue surface; Figure 1b). However, the 2017 annual mean subglacial runoff transport estimated from RACMO (0.11 mSv) agrees within uncertainty with the observationally derived estimate from Schaffer et al. (2020), and we expect the seasonal cycle of subglacial runoff to be very similar to that of total surface melt.

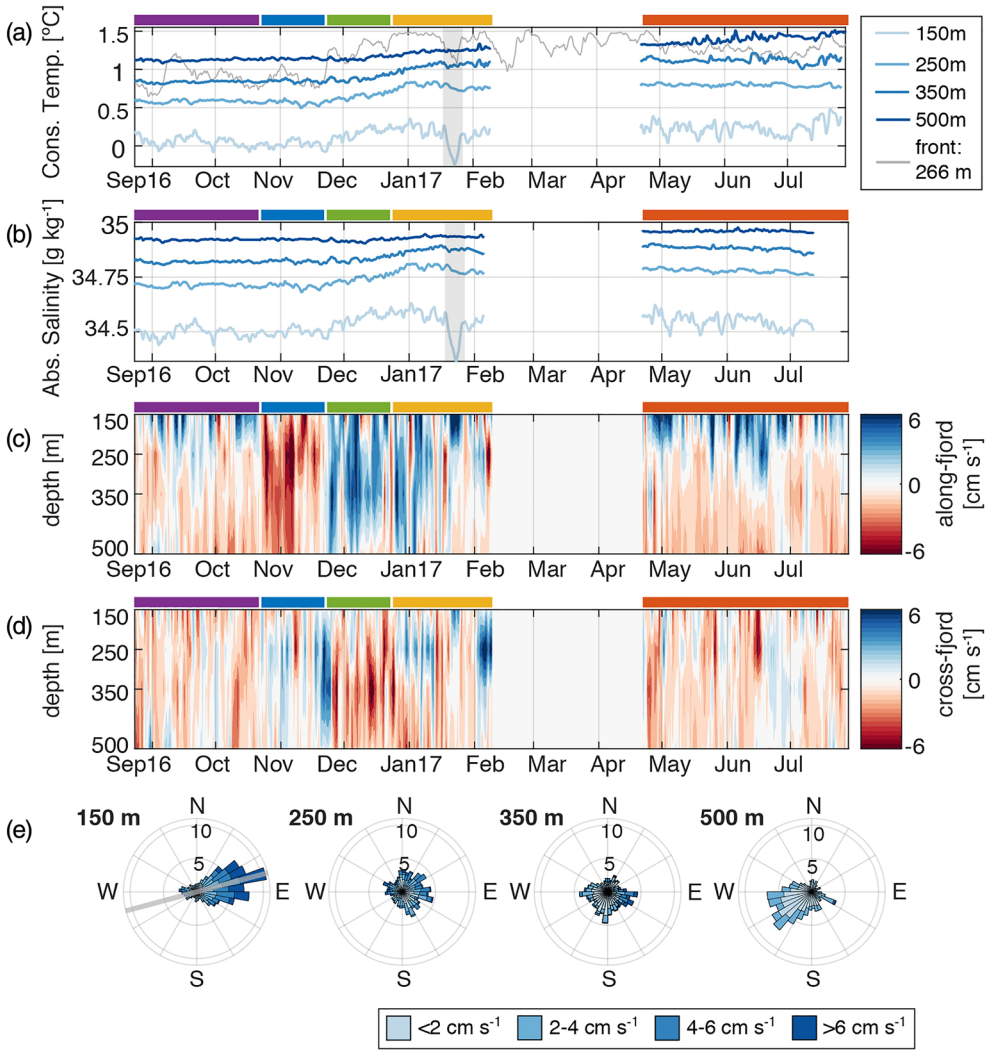

Figure 3. Low-pass filtered ITM data from the 79NG ice tongue cavity. (a) Timeseries of conservative temperature at the ITM (each depth, blue) and PF (266 m, gray). (b) Timeseries of absolute salinity at the ITM (each depth, blues). Shaded regions in (a) and (b) indicate the cold pulse discussed in section 3.3. (c) Along-fjord velocity at the ITM (rotated onto 150 m major axis of variability; see gray line in (e)). Positive velocities (blue) are directed toward the pinned front. (d) Cross-fjord velocity at the ITM (150 m minor axis). This direction corresponds approximately to flow toward and away from Dijmphna Sund, with positive velocities (blue) toward Dijmphna Sund. Velocities in (c) and (d) are vertically interpolated with the current meter depths indicated by tick marks on the y-axis. Colored lines above (a) and (d) indicate the duration of each time period shown in Figure 5. (e) Velocity roses (not rotated) showing time percentage of current directions at each depth. Shading indicates current speed. The light gray line on the 150 m rose indicates the major axis of variability (i.e., inferred along-fjord direction).

3. Results

3.1. Water Masses in the 79NG Cavity

The vertical structure of water masses at the time of ITM deployment in August 2016 is consistent with previous observations, with relatively cold fresh water overlying warmer saline AIW present at depth (Figures 2a and 2b). Temperature increases over the full water column depth, so our mooring record from 500 m likely does not capture the maximum temperatures present in the cavity. At 250 m and below, the temperature-salinity (T-S) properties in the initial profile fall approximately along a melt line relative to the deep AIW properties (Figure 2c). The melt line, or Gade slope, represents the expected temperature and salinity of glacially modified water formed when the heat for ice melt is supplied from a single endmember water mass (in this case, AIW) (Gade, 1979). The T-S property distribution suggests that the cavity is filled mainly with a mixture of AIW and ice tongue basal melt. (We note that the mixing line slope between AIW

Table 2
Variability in Conservative Temperature (CT) and Absolute Salinity (AS) Observed at Ice-Tethered Mooring in 79 North Ice Tongue Rift, August 2016 to July 2017

Depth	Time period[a]	CT mean[b] (°C)	CT trend[c] (°C month^{-1})	AS mean (g kg^{-1})	AS trend (g kg^{-1} month^{-1})
150 m	*Full record*	**0.15 ± 0.12**	**0.02 ± 0.01**	**34.53 ± 0.04**	—
	Aug–Oct	0.05 ± 0.06	—	34.50 ± 0.02	—
	Oct–Nov	0.03 ± 0.04	—	34.50 ± 0.02	—
	Nov–Dec	0.13 ± 0.09	—	34.55 ± 0.04	—
	Dec–Feb	0.16 ± 0.12	—	34.55 ± 0.06	—
	Apr–Jul	0.22 ± 0.07	—	34.55 ± 0.03	—
250 m	*Full record*	**0.70 ± 0.10**	**0.02 ± 0.01**	**34.75 ± 0.03**	—
	Aug–Oct	0.58 ± 0.02	—	34.71 ± 0.01	—
	Oct–Nov	0.56 ± 0.03	—	34.71 ± 0.01	—
	Nov–Dec	0.63 ± 0.04	0.22 ± 0.08	34.74 ± 0.01	0.20 ± 0.08
	Dec–Feb	0.77 ± 0.04	—	34.79 ± 0.02	—
	Apr–Jul	0.80 ± 0.02	—	34.78 ± 0.01	-0.01 ± 0.00
350 m	*Full record*	**0.98 ± 0.13**	**0.04 ± 0.01**	**35.85 ± 0.03**	**0.01 ± 0.00**
	Aug–Oct	0.84 ± 0.01	—	34.82 ± 0.00	—
	Oct–Nov	0.85 ± 0.02	—	34.82 ± 0.01	—
	Nov–Dec	0.87 ± 0.03	—	34.83 ± 0.01	—
	Dec–Feb	1.04 ± 0.05	0.07 ± 0.05	34.87 ± 0.01	0.07 ± 0.05
	Apr–Jul	1.12 ± 0.03	—	34.88 ± 0.01	—
500 m	*Full record*	**1.25 ± 0.12**	**0.03 ± 0.00**	**34.94 ± 0.02**	—
	Aug–Oct	1.12 ± 0.01	—	34.92 ± 0.00	—
	Oct–Nov	1.14 ± 0.01	—	34.92 ± 0.00	—
	Nov–Dec	1.14 ± 0.02	—	34.92 ± 0.01	—
	Dec–Feb	1.23 ± 0.04	0.06 ± 0.03	34.93 ± 0.01	0.07 ± 0.02
	Apr–Jul	1.38 ± 0.05	0.04 ± 0.02	34.96 ± 0.00	0.04 ± 0.02

[a]Time periods refer to date ranges indicated in Figures 3a and 3b. [b]Range given is one standard deviation. [c]Trends listed if significant at the 95% confidence level.

and cold, fresh PW present on the continental shelf is similar to the melt line slope. We provide additional evidence to support the interpretation that this is glacially modified water in section 3.2.) Mixing with subglacial runoff, which is assumed to enter the ocean at the local freezing temperature with salinity 0 g kg^{-1}, is represented by the runoff line. At 150 m, T-S properties initially fall between the melt line and the runoff line, indicating that there is runoff in the upper water column (Figure 2c). Waters in August 2016 are consistently warmer relative to the 1998 and 2009 observations over the observed water column (Figures 2a and 2b).

Comparison with the initial properties at the PF site indicates the presence of similar water masses inside the cavity and outside the calving front, with a maximum temperature of 1.35°C at the ITM (713 m) and 1.37°C at PF (314 m; Figure 2a). T-S properties at PF fall along the melt line below 245 m and between the melt and runoff lines between that depth and the shallowest mooring instrument at 206 m, suggesting that the ocean properties recorded by the mooring initially contain glacially modified waters, including subglacial runoff, from the cavity (Figure 2c). Distinguishing between glacially modified waters and PW is particularly challenging on the shelf, but the overlap of properties at the PF site below 200 m with properties in the cavity on the T-S diagram suggests that there is not significant PW at these depths, in agreement with past observations (Wilson & Straneo, 2015).

Over the course of the ITM record, AIW temperature and salinity observed at 500 m increase from 1.12°C to 1.49°C and from 34.92 to 34.95 g kg^{-1}, respectively (Figures 3a and 3b). Smaller increases are observed at the shallower depths. Increasing temperature and salinity are first observed at 150 and 250 m in late November

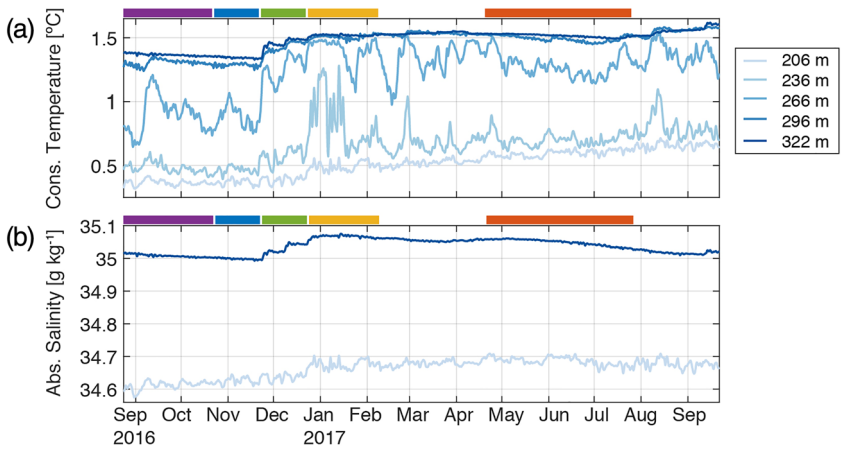

Figure 4. Low-pass filtered timeseries of (a) conservative temperature and (b) absolute salinity at PF (each depth, blues). The colored lines correspond to those in Figures 3a–3d for comparison to the ITM timeseries.

2016 and at 350 m and 500 m beginning in December 2016. Mean and variability in properties at each depth for the time periods indicated by the colored lines above Figures 3a and 3b are listed in Table 2.

The timeseries of PF temperature and salinity (Figures 4a and 4b) are broadly similar to the ITM timeseries. Variability in PF temperature and salinity are relatively small from August to late November 2016, except at 266 m, where temperature ranges from 0.65°C to 1.21°C. This is likely because it is initially located in a strong thermocline (Figure 2a), making temperatures near that depth particularly sensitive even to small isopycnal displacements. At 322 m, which likely reflects AIW properties, temperature increases from 1.38°C in August 2016 to 1.52°C in July 2017, warming further to 1.61°C through September 2017 (Figure 4a). Connections between the ocean property variability at the ITM and PF locations and their interactions with the circulation are discussed in depth in section 3.3.

3.2. Cavity Circulation and Exchange with Continental Shelf

Time-mean and standard deviation of current speeds observed at the ITM ranged from $4.2 \pm 2.5\,\mathrm{cm\,s^{-1}}$ at 150 m to $2.3 \pm 1.3\,\mathrm{cm\,s^{-1}}$ at 500 m. Tidal currents were estimated using T_Tide harmonic analysis (Pawlowicz et al., 2002). Tides appear to be primarily barotropic. The largest reconstructed tidal velocity was the M2 semidiurnal lunar tide, with magnitude $1.4 \pm 0.1\,\mathrm{cm\,s^{-1}}$ at all depths. No other semidiurnal or diurnal tidal constituents were associated with velocities greater than $0.5\,\mathrm{cm\,s^{-1}}$. Tidal currents account for as little as 7.4% of velocity variance at 150 m and up to 26.5% of variance at 500 m. Velocities were low-pass filtered (see section 2) for analysis of the subtidal circulation.

At 150 m, the major axis of current variability is oriented toward 15°N and explains 68.8% of the total velocity variance at that depth (Figure 3e). This direction corresponds to along-fjord velocities in the main branch of the fjord, that is, toward the pinned front to the east (Figure 1a; solid white arrow). Velocities at all depths are rotated onto this axis for analysis of the along- and cross-fjord circulation (Figures 3c and 3d).

Time-mean along-fjord velocities are consistent with a weak overturning circulation, with mean outflow of $2.1 \pm 0.3\,\mathrm{cm\,s^{-1}}$ at 150 m ($p < 0.001$) and inflow of $0.4 \pm 0.2\,\mathrm{cm\,s^{-1}}$ at 500 m ($p = 0.02$) (Figure 5a; see Appendix A for calculation of standard error of the mean). This mean flow is qualitatively consistent with the circulation pattern inferred from hydrography, indicating inflowing AIW from the continental shelf at depth and shallow export of glacially modified water (e.g., Wilson & Straneo, 2015). However, the main fjord width ranges from 20 km at the grounding line to 30 km at the mouth, which is 5–10 times wider than the internal deformation radius of 3–4 km (computed from the August 2016 buoyancy frequency profile; Chelton et al., 1998), and the main inflow is localized within a 2 km wide channel near the center of the pinned front (Figure 1a; Schaffer et al., 2020). Thus, it is likely that significant variations in current amplitude and direction exist across the fjord. Furthermore, bathymetry, which is poorly known beneath the ice tongue (Mayer et al., 2000), likely plays a role in steering the flow. The current meters measure only at discrete depths, and the deepest instrument is above the densest AIW and approximately 200 m above the seafloor (720 m; Figures 2a and 2b), so it is likely that our observations do not capture the strongest inflow.

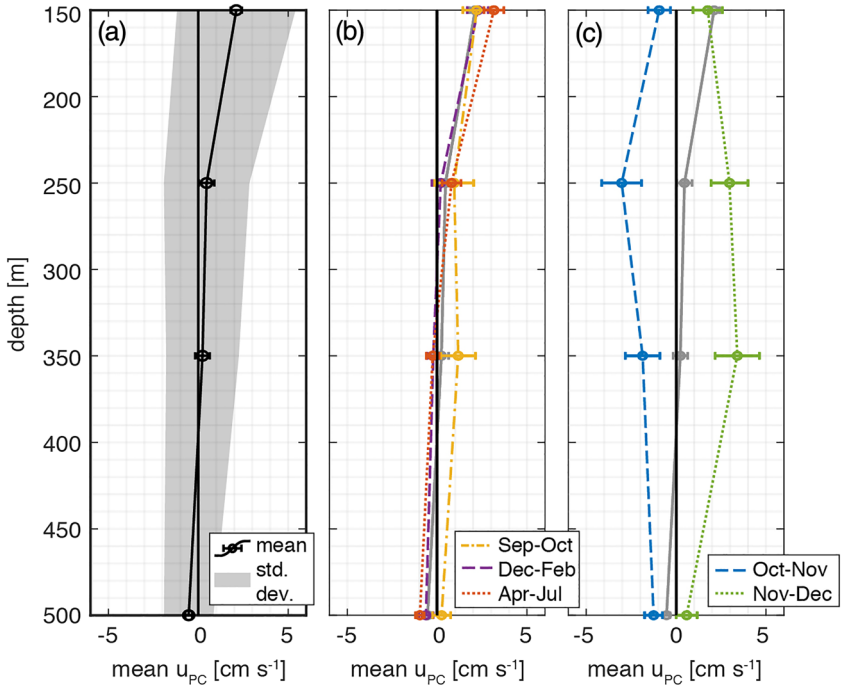

Figure 5. Time-mean along-fjord velocity at each ITM depth for (a) the full timeseries and (b, c) the time periods indicated by the colored bars in Figure 3. Positive (negative) velocities correspond to inferred outflow (inflow) direction. Error bars indicate the standard error of the mean (see Appendix A). The shaded range indicates the standard deviation. Time periods in (b) and (c) were selected to highlight transitions between the circulation modes discussed in section 3.2 and range in length from 1 to 3.5 months. The full record mean and standard error is plotted in gray (solid line) on each panel for comparison.

Two distinct modes of circulation are observed in the along-fjord velocities. During the first 2 months of the record, the time-mean circulation closely reflects the mean overturning pattern of the full record (Figure 5b). A second, more barotropic mode is observed from late October to late December 2016 with inflow at all depths in late fall (late October through late November) and outflow from the cavity in early winter (late November through late December, Figure 5c). During these times, the strongest observed velocities are at the mid-depth instruments, 250 and 350 m. In mid-winter (late December through February), there is outflow at 150 and 350 m, with means not significantly different from zero at the other depths (Figure 5b). Following the gap in the record in late winter and early spring, the final 3.5 months of the timeseries show a slightly enhanced overturning with inflow at 500 m and outflow at both shallower instruments (Figure 5b).

Variability in current direction is large at 250 and 350 m (Figure 3e), and mean along- and cross-fjord velocities over the full timeseries are not significantly different from zero at either depth (Figure 5a). The mid-depth currents have intervals (days to weeks) of significant flow in all directions, including predominantly southward (negative cross-fjord) flow during August (250 and 350 m) and September (350 m) and northward (positive cross-fjord) flow during mid-November (both), mid-December, and mid- to late-January (250 m) (Figure 3d). These time periods alternate with periods of flow in the along-fjord direction, suggesting that there may be intermittent exchange with Dijmphna Sund at these depths.

Assuming that the along-fjord velocity component is representative of the exchange flow through the eastern pinned front with inflow at 500 m and outflow at 150 m, we estimate a time scale for cavity renewal. Based on the mean velocity profile (Figure 5a), we assume that there is a middle layer of no net flow extending at least from 250 to 350 m depth. We also impose a balance between inflow and outflow such that there is no net transport. The possible inflow and outflow layer thicknesses are thus constrained by this balance, in addition to the physical boundaries of the ice base, "stagnant" middle layer, and seafloor. We approximate that the outflow observed at 150 m represents the average over an upper layer with thickness between 50 and 75 m, and the inflow observed at 500 m represents the average over a layer with thickness 200 to 275 m.

Under these simplified assumptions and given these ranges of layer thickness, the estimated cavity residence time calculated from the mean overturning velocities is between 255 and 380 days. Repeating the calculation for the time-mean velocities from April to July, when the overturning is slightly strengthened (Figure 5b), reduces the estimated exchange time scale to between 175 and 265 days. These estimates, based on the first direct observations of cavity currents, are consistent with a previously published estimate of 110 to 320 days based on a cavity heat budget assuming a steady state balance between heat advection and melting (Wilson & Straneo, 2015). A more recent estimate based on volume transport estimates from moored current meters at the cavity gateways gave an average residence time of 162 days, below the range calculated here (Schaffer et al., 2020). This suggests that the ITM observations may not reflect the full overturning strength, either due to the location or the low vertical resolution of the current meters.

3.3. Characteristics and Timing of 2016–2017 Ocean Property Variability

Warming of waters at the ITM is observed at all depths over the course of the record (Figure 3a; Table 2). The asynchronicity of the warming at different depths indicates multiple mechanisms and time scales of ocean property variability. We present evidence of large-scale events that impact properties on the continental shelf and inside the cavity concurrently. Our analysis suggests that shallow properties at the ITM respond quickly to changes on the shelf via propagation of internal waves, while the properties of inflowing AIW observed primarily at 500 m vary more slowly. Finally, the outflowing glacially modified water adjusts to the change in inflow properties with some lag and is also influenced seasonally by subglacial runoff (see section 3.4).

In late November 2016, the 266 m temperature at PF warms abruptly by about 0.4°C within 2 days (see section 3.1; Figure 3a). The onset of warming within the cavity is then observed at the ITM at 150 and 250 m, with a lag of about 1 day. This coincides temporally with a shift in circulation, where the along-fjord currents reverse from predominantly inflow to predominantly outflow (Figure 3c). Warming of at least 0.15°C is observed at 150, 250, and 350 m by the end of December 2016 (Figure 3a). This late fall warming signal is not observed at 500 m, suggesting that it is confined above the sill depth of approximately 480 m (Schaffer et al., 2020). In T-S space, observed properties during this period of warming vary approximately parallel to the melt line at 150 and 250 m (Figures 6a and 6b; green arrows). At 350 m, the variation in T-S properties is initially close to the melt slope but becomes steeper later in December 2016 (Figure 6c; green arrow). The melt slope is similar to the slope of the initial T-S properties observed at the ITM (see section 3.1). Based on the August 2016 stratification, we speculate that this warming and salinification correspond to upward isopyncal displacement of about 50 m at the three shallower instruments (Figures 2a and 2b).

The lag relationship between this warming signal at the two moorings suggests that it propagated into the cavity from the continental shelf. The mode one internal wave phase speed calculated using the August 2016 profile of buoyancy frequency N^2 (Chelton et al., 1998) at the ITM site is on the order of 50 cm s^{-1}, resulting in an approximate travel time of 19 hr between the mooring at the ice front and the ITM. (N^2 ranges from 0.5 to 2×10^{-5} s^{-2} between 150 and 350 m.) The current velocities at the ITM at the onset of this warming are order 1 cm s^{-1}, yielding an advective time scale of days to weeks between the ice front and the ITM; furthermore, the along-fjord flow during this period is directed out of the cavity (Figure 5c). The T-S characteristics of the warming signal, the brief lag between its arrival at the two moorings, and the simultaneous outflowing currents suggest a vertical displacement of isopycnals on the continental shelf that likely propagated into the cavity as a wave, rather than advection of a different water mass. This indicates an effective mechanism by which above-sill ocean properties within the cavity may respond to changes on the continental shelf on time scales of hours to days. Because the warming persists at both the ITM near the northern edge of the cavity and the PF site near the southern edge of the ice front, it likely affects the cavity properties over much of its width in the vicinity of the front where the ice draft is relatively shallow.

Higher frequency temperature and salinity variability observed at the ITM, on time scales of days to weeks, is greatest at 150 m (see section 3.1; Figures 3a and 3b). Similar to the warming signal described above, this variability is characterized primarily by fluctuations parallel to the melt line in T-S space (Figure 6a), suggesting that it reflects vertical motion of isopycnals. A notable exception to this pattern occurs over 8 days in late January 2017, when the coldest and freshest conditions of the entire record are observed at 150 m (Figures 3a and 3b; shaded). The strongest observed flow occurs at the same time, with a mean current velocity greater than 10 cm s^{-1} toward the northeast (Figures 3c and 3d). In T-S space, this cooling and freshening signal falls above the meltwater mixing line (Figure 6a; gray-circled points). As the properties depart the mixing line, they instead fall close to the August 2016 T-S profile, with the minimum temperature (-0.24°C)

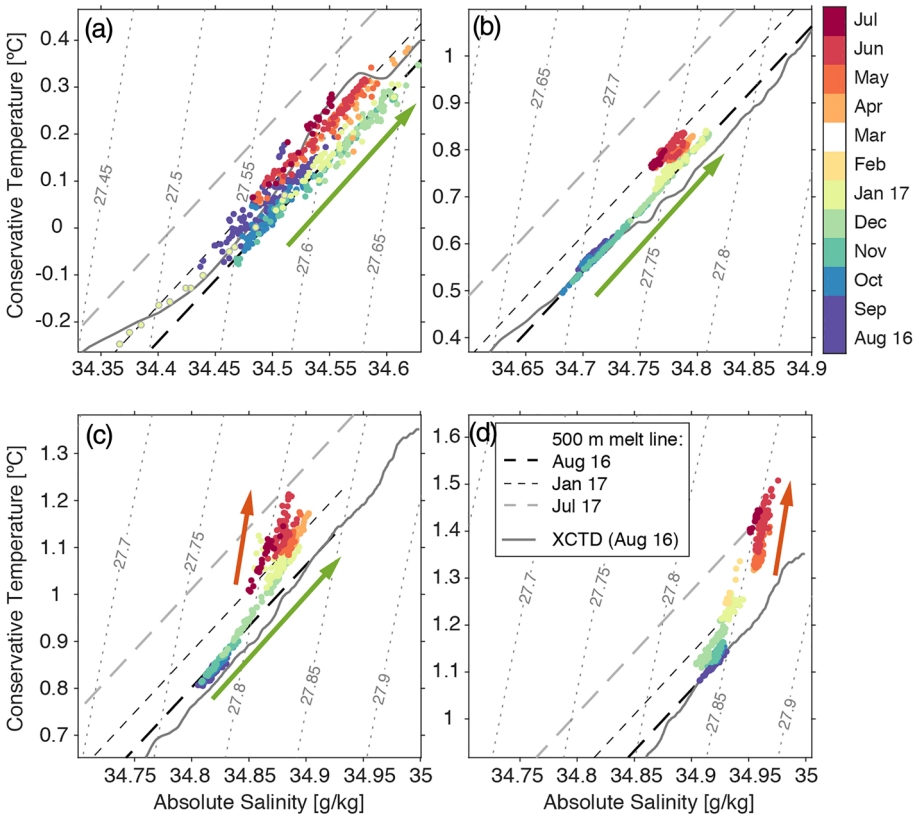

Figure 6. Time-varying (2 points per day) temperature versus salinity plots for (a) 150 m, (b) 250 m, (c) 350 m, and (d) 500 m at the ITM. The initial XCTD profile from August 2016 is plotted as a solid gray line. The dashed lines indicate the Gade slope relative to the 500 m water mass properties in August 2016 (thick black), January 2017 (thin black), and July 2017 (gray). Green arrows (parallel to the melt line) in (a) to (c) indicate trajectory of warming during November–December 2016. Red arrows (parallel to isopycnals) in (c) and (d) indicate trajectory of AIW warming during January–July 2017. Gray circled points in (a) correspond to the gray shaded time period of January 2017 in Figures 3a and 3b.

and salinity (34.37 g kg^{-1}) (Figures 3a and 3b) corresponding to properties observed at approximately 125 m depth (Figures 2a and 2b). Cooling at 266 m depth at PF, which likely indicates deepening of the pycnocline, is observed beginning a few days before the onset of the ITM cooling event (Figure 3a). This suggests that the transient cooling and freshening observed at 150 m at the ITM in January 2017 is linked to a larger scale event that also affects the continental shelf. Potential mechanisms are discussed further in section 4.1.

In contrast to the fall 2016 warming and high-frequency variability, the warming observed at 500 m beginning in late December 2016 and continuing through summer 2017 occurs primarily along the 27.86 isopycnal (Figure 6d; red arrow), indicating advection of a warmer water mass at the ITM location. During spring 2017, the T-S properties at 350 m similarly deviate from the melt line and become more similar to the properties at 500 m (Figure 6c), and the mean 350 m current direction is into the cavity during this period (Figure 5b), suggesting thickening of the inflowing AIW layer at the same time as it is warming and freshening. The 150 and 250 m properties continue to warm through the end of the record, but high frequency variations in properties are still primarily parallel to the melt slope, which is consistent with the interpretation that these outflowing waters are glacially modified AIW (Figures 6a and 6b). This warming and freshening of the AIW properties is not observed at PF until July 2017 (Figure 4), indicating that while ocean properties at the PF location may be linked strongly to above-sill cavity properties, it is isolated from the major AIW inflow pathway (Figure 1a).

The AIW observed at the ITM location at 500 m warmed by 0.4°C between late December 2016 and June 2017 (Figure 3a). In July 2018, observed temperatures at 500 and 150 m were close to their 2016–2017 maxima, while waters at 250 and 350 m had warmed beyond their July 2017 maxima by 0.18°C and 0.05°C,

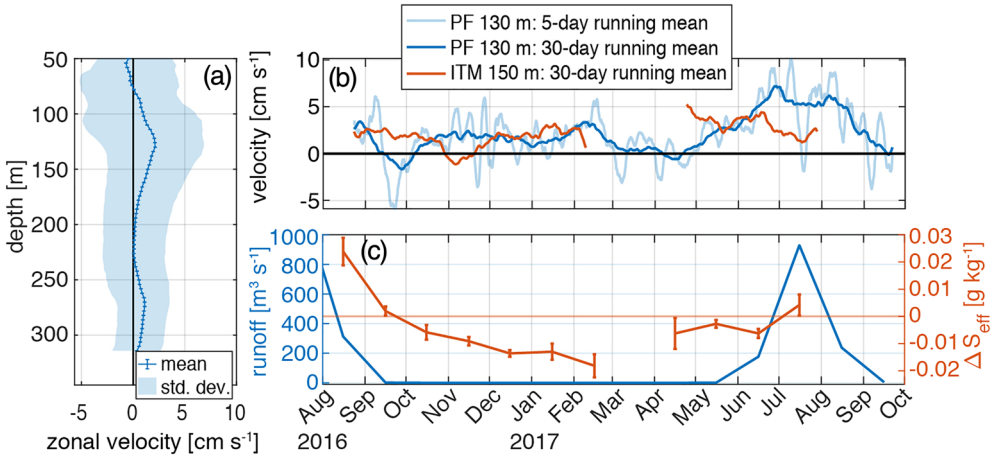

Figure 7. (a) Depth profile of time mean zonal velocity at the PF site. Error bars indicate the standard error of the mean; the shaded area indicates the standard deviation. (b) Timeseries of 130 m zonal velocity at the front mooring, 30-day running mean (dark blue) and 5-day running mean (light blue), and 150 m along-fjord velocity at the ITM, 30-day running mean (red). (c) Monthly average of subglacial runoff volume flux from RACMO (blue). Monthly average of difference in effective salinity between 150 and 250 m ΔS_{eff} at ITM (red). If positive, indicates that waters at 150 m are fresher relative to 250 m than would occur purely through increasing basal melt concentration. Error bars indicate standard error of the mean (see Appendix A).

respectively (Figure 2a). While the 150 m temperature was highly variable, with a range overlapping all previous CTD measurements, for the duration of the mooring record, the 350 and 500 m temperatures were consistently higher than in any observations prior to 2016. Furthermore, the magnitude of subannual AIW temperature variability observed at 500 m is smaller than previously observed interannual variability, indicating that AIW in the 79NG cavity has warmed since 1998.

The change in AIW inflow properties provides another possible observational constraint on cavity renewal time scale. At the end of the ITM record (mid-July 2017), T-S properties at 250 m fall along a melt line relative to the 500 m properties in mid-January 2017 (Figure 6b). This is consistent with our interpretation that the inflowing AIW observed at the ITM is carried toward the 79NG grounding line, is modified through basal melt of the ice tongue, and is exported at shallower depths. Furthermore, the timing suggests an approximately 6-month, or 180-day lag between the arrival of an inflowing parcel of AIW at the ITM location and its subsequent export through the melt-driven circulation. This estimate falls within the lower end of residence time scales estimated from mean currents observed between April and July 2017 (see section 3.2), agreeing well with the estimate in Schaffer et al. (2020). (Properties observed at 150 m are not mentioned here because they are likely more strongly influenced by runoff modification during this time period; see section 3.4.)

3.4. Impacts of Seasonally Variable Runoff

We can find evidence of mixing with subglacial runoff on T-S plots by identifying waters that are anomalously fresh compared to a melt slope, as described in section 3.1. To consider the temporal variability in subglacial runoff concentration, we define an "effective salinity" as the salinity where a melt slope intersects the freezing line in T-S space. Changes in the effective salinity of glacially modified waters therefore reflect property changes that cannot be accounted for solely through changing the proportion of basal melt, such as the addition of surface runoff, though it is also affected by variability in the AIW endmember properties.

We show the difference in effective salinity between 150 and 250 m (ΔS_{eff}) at the ITM in Figure 7c (red). Assuming that waters at 250 m are not modified by mixing with subglacial runoff, which they are not in August 2016 (Figure 2b) and that waters at 150 and 250 m respond to changes in AIW properties at the same rate, we expect the addition of runoff at 150 m to manifest as a positive value of ΔS_{eff}. In late August 2016, when we deduce the presence of runoff at 150 m from the temperature and salinity profiles at the ITM location, ΔS_{eff} is at a maximum value of 0.024. ΔS_{eff} remains greater than 0 in September 2016 and is again positive in July 2017 ($p < 0.001$). This timing is consistent with the timing of summer ice sheet surface melt in the 79NG catchment area derived from RACMO (Figure 7c, blue Noël et al., 2018; Slater et al., 2019). We thus interpret ΔS_{eff} as a proxy for runoff concentration at 150 m the ITM.

Surface melt volume explains 80% of variability in ΔS_{eff} with a 1-month lag (correlation $R^2 = 0.80$, $p = 0.002$). Such a lag in the response of observed runoff concentration to surface melt is reasonable due to the time needed for meltwater to travel through the glacial hydrologic system to the grounding line and the additional advection time from the grounding line to the ITM. At the April–July mean 150 m current speed of 3.1 cm s^{-1}, a water parcel would be advected from the grounding line to the ITM location in 22 days. An analogous property signal is difficult to identify in the timeseries from the PF mooring due to the low vertical resolution of salinity sensors, but runoff was inferred to be present at the PF site above 245 m in the August 2016 observations (Figure 2c).

At the PF site outside the ice front, the mean zonal current velocity at 130 m, inferred to reflect outflow from the cavity, is above 5 cm s^{-1} throughout June–August 2017, significantly higher than the September 2016 to May 2017 average of 1.1 cm s^{-1} (Figure 7b). This acceleration could be associated with an increased export of glacially modified waters from the cavity. In contrast, there is no significant seasonal change in export velocity at the ITM through the end of the record. Localization of an outflowing plume of buoyant glacially modified water toward the southern side of the 79NG cavity is consistent with the expected effect of the Coriolis force, even in the presence of basal channels (e.g., Millgate et al., 2013). These results suggest that melt runoff is present in shallow waters throughout the cavity during the summer months and likely drives seasonal circulation changes by increasing the volume flux from the cavity, with the main export concentrated near the southern edge of the cavity.

3.5. Basal Melt Variability

Remote sensing, in situ radar, and hydrographic analyses have found that ice shelf basal melt rates are highly variable in space (e.g., Langley et al., 2014; Stewart et al., 2019; Wilson et al., 2017) and additionally suggest significant temporal variability on daily to interannual time scales (e.g., Adusumilli et al., 2018; Mayer et al., 2018; Schaffer et al., 2020; Stevens et al., 2020; Washam et al., 2019). We use the ITM observations and an established model of basal ice melt (e.g., Jenkins et al., 2010) to generate independent estimates of melt rate variability through two different approaches. First, we use the full record to calculate a timeseries of local basal melt at the ITM site. We then use a plume model (e.g., Jenkins, 2011; Mayer et al., 2018; Slater et al., 2017) to estimate the subannual change in basal melt in the vicinity of the grounding line associated with the observed warming of deep AIW.

We employ the three-equation formulation of Jenkins et al. (2010, Equations 11–13) to calculate the local basal melt rate, using the unfiltered timeseries of temperature, salinity, and current speed (i.e., the square root of summed squares of the along- and cross-fjord velocities) from the ITM at 150 m depth, which is closest to the depth of the ice base (Figure 8a). The melt rate calculation additionally relies on the Thermal Stanton number St_T, a nondimensional parameter that depends on a heat transfer coefficient and the drag coefficient at the ice shelf base, both of which are uncertain. We use a range of values for St_T from 4.5×10^{-4} to 1.3×10^{-3}, derived from observations under an Antarctic ice shelf (Davis et al., 2018; Stanton et al., 2013), to estimate uncertainties for the computed melt rates, represented by the gray shading in Figure 8b.

We estimate a time-mean melt rate of 8.3–23.1 m yr^{-1}, which is consistent with the Wilson et al. (2017) estimate in the vicinity of the 79NG rift (6.5 ± 2.8 m yr^{-1}). We discuss temporal variability of the timeseries calculated with $St_T^* = 8.5 \times 10^{-4}$ (Figure 8b; black line), but the relative values are independent of the choice of St_T, assuming its value is constant in time. The time-mean melt rate for St_T^* is 15.7 m yr^{-1} with standard deviation 9.3 m yr^{-1} (60%), revealing considerable temporal variability. The variability of the timeseries of basal melt closely resembles the variability in current speed, which is expected, because the variability in speed is much greater than the variability in thermal forcing on time scales of days to weeks (Figures 8a and 8b). However, the January–July 2017 mean (17.9 ± 1.0 m yr^{-1}) is 33 ± 20% higher than the August–November 2016 mean (13.6 ± 1.3 m yr^{-1}) (Figure 8b; see Appendix A for calculation of the standard error of the mean). We find that this significant increase in melt rate ($p = 0.001$) cannot be explained by changes in current speed and attribute it to sustained ocean warming.

This approach relies on some key assumptions. We assume that currents at the ITM location are not affected by drag from the ice base, and crucially, that despite being below a rift, these observations are representative of conditions at the ice tongue base nearby. This can be justified to an extent by the fact that the rift is relatively narrow (see section 2), but it is very likely that the salinity adjacent to the ice base is lower than what is observed at the ITM due to the accumulation of buoyant meltwater. As a result, this method

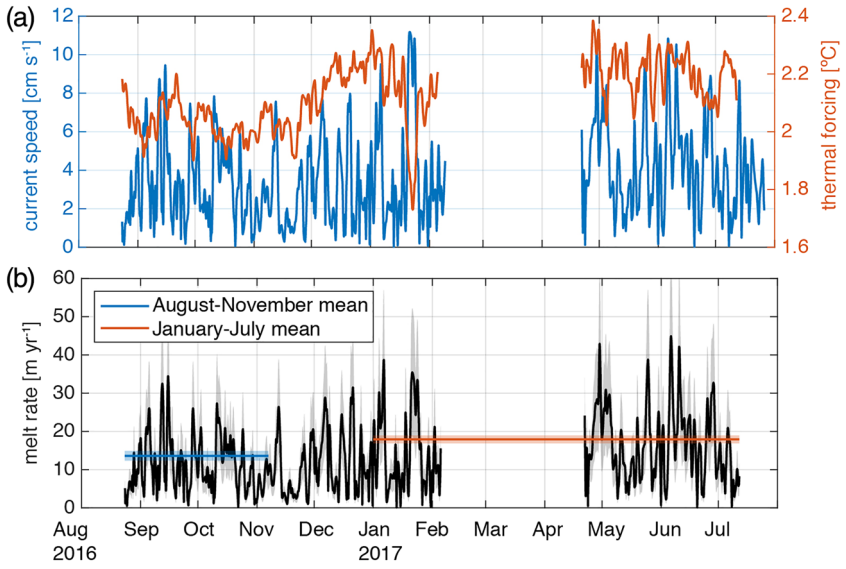

Figure 8. (a) Timeseries of horizontal current speed at 150 m (blue) and thermal forcing $T - T_f$ (red). (b) Timeseries of computed basal melt rate (black). The black line is calculated using $St_T^* = 8.5 \times 10^{-4}$; gray shading indicates the range of melt rates resulting from varying St_T between 4.5×10^{-4} and 1.3×10^{-3}. The August–November (blue) and January–July (red) time means for St_T^* are plotted over the corresponding time periods, with shaded bars indicating the standard error of each mean value (see Appendix A).

is likely to overestimate melt rates, and the reported magnitudes should be interpreted with particular caution. Nevertheless, we note that the resulting estimate of mean melt rate agrees within uncertainty with the independent result of Wilson et al. (2017) and focus our interpretation on the additional information about relative temporal variability provided by this approach.

At 79NG, the largest overall melt rates occur in the vicinity of the grounding line, where the ice base is in contact with the warmest water and the freezing point is depressed due to higher pressure (Wilson et al., 2017). We use the one-dimensional, nonrotational line plume model given by Slater et al. (2017; Equations 1 and 2) to estimate the impact of the observed warming on basal melt over the region of the ice tongue up to 12 km downstream of the grounding line, where the ice tongue base slope is steepest. The ice tongue base in this region is between 250 and 600 m deep (Wilson et al., 2017). We force the plume model with monthly mean T-S profiles observed at the ITM, under the assumption that ocean properties observed at the ITM are representative of waters reaching the grounding zone at equivalent depths. We exclude subglacial runoff input at the grounding line to isolate the effect of ocean warming, but note that it is expected to seasonally enhance basal melt. Unconstrained model parameters in addition to St_T, including the entrainment coefficient, affect the absolute magnitudes of melt simulated by the plume model; thus, we report only the relative change in melt rates, which is robust to variation of these parameters. Using October 2016 as a baseline, we estimate that 2016–2017 ocean warming drives a 14 ± 2% increase in basal melt rate, which, if sustained, could drive further thinning of the ice tongue grounding zone.

4. Discussion

The ITM record represents the first observations of temporal variability in the properties of waters and currents in the 79NG cavity on hourly to subannual time scales. The mean overturning circulation observed inside the 79NG cavity, together with the ocean properties, are consistent with the glacial melt-driven estuarine circulation inferred by Wilson and Straneo (2015), and comparison with the record from Schaffer et al. (2020) suggests that circulation and properties at the ITM location are linked to variability of the hydraulically controlled inflow. Our results suggest that several processes likely interact to drive the complex and variable ocean circulation in the cavity that determines 79NG ice tongue basal melt. In the following, we discuss potential mechanisms of the observed variability and their implications for the ice tongue.

4.1. Continental Shelf-Driven Variability

The abrupt warming of shallow waters in November 2016 is observed first at the mooring outside the front, suggesting a mechanism driven by processes on the continental shelf. A recent study of mooring records from the shelf shows large-scale warming and thickening of the AIW layer during the same time period (Schaffer et al., 2020), indicating that both the shallow and deep warming signals observed at the ITM were likely driven by this external variability. Schaffer et al. (2020) show that AIW inflow into the 79NG ice tongue cavity is concentrated below 350 m depth and is hydraulically controlled by a shallow sill outside the pinned front. Beginning in November 2016, thickening of the AIW layer upstream of the sill by 50 m drove enhanced AIW transport into the cavity. This finding supports our interpretation that the initial warming of the shallow waters was driven by the propagation of the isopycnal shoaling signal from the shelf as the layer thickened. The subsequent warming of the AIW at 500 m with a lag of approximately 1 month is thus understood to be the advection of the warmer AIW from the pinned front to the ITM location.

A warm anomaly in Atlantic waters observed on the continental slope in the mid-2000s may offer an analogue to the AIW warming observed in the 79NG cavity between January and July 2017 (Beszczynska-Möller et al., 2012). Between hydrographic surveys in summer 2005 and 2006, the recirculating Atlantic water (RAW) layer in the EGC warmed by 0.25°C and freshened by about 0.02 psu. Similarly, AIW observed at 322 m at PF from July through September 2017 was observed to warm by about 0.1°C and freshen by as much as 0.02 g kg^{-1}, resulting in a decrease in density of 0.02 kg m^{-3} (Figure 2c). de Steur et al. (2014) found that the mid-2000s warming caused a similar density anomaly, which was linked to thickening of the RAW layer on the continental slope. The anomalous warming and thickening of the RAW were both reversed in the following years (through 2011), though the long-term warming trend appeared to persist (Beszczynska-Möller et al., 2012; de Steur et al., 2014). This suggests the possibility of a reversal of the relatively rapid 0.4°C warming observed by the ITM at 500 m during 2017 and a return to the more gradual warming suggested by the earlier observations.

There is noticeable variability in the currents and ocean properties observed at the ITM on time scales of days to weeks, with larger variance at shallower depths (Figures 3a–3d), though this is not associated with a significant spectral peak. Münchow et al. (2020) find that topographic Rossby waves generated by offshore Ekman pumping propagate along Norske Trough with periods of 6–20 days. This could drive oscillations in the AIW layer thickness at the sill outside the pinned front, which may result in isopycnal oscillations in the cavity as suggested above, as well as modulating the inflow strength and causing variability in currents observed at the ITM (Schaffer et al., 2020).

In particular, internal waves on the continental shelf offer a possible explanation for the strong shallow outflow observed at the ITM during the January 2017 cooling and freshening event discussed in section 3.3. Cooling observed at PF (Figure 3a) and results from Schaffer et al. (2020) indicate that this event is preceded by lowering of the pycnocline on the shelf by about 50 m. Their results show enhanced outflow through the pinned front, with the peak roughly coinciding with the initiation of the anomaly observed at the ITM, suggesting that this event could be part of a larger scale rearrangement of circulation in response to shelf forcing. However, the dominant processes driving current variability in the cavity remain unclear, and there are numerous possible explanations for this signal. For example, Washam et al. (2019) observe qualitatively similar events beneath Petermann Gletscher, that is, cold, fresh pulses with increased current speeds, and attribute these to intermittent releases of subglacial runoff from the grounding line. Such an outflow from beneath the ice tongue, if sufficient in magnitude and localized on the southern side of the cavity due to Coriolis (see section 3.4), could be responsible for the depression of the pycnocline outside the pinned front before the corresponding signal was observed at the ITM. The influence of subglacial runoff at 79NG is discussed further in the next section.

4.2. Glacier and Cavity Variability

We find evidence that seasonal subglacial discharge of ice sheet surface runoff affects cavity circulation and temperature-salinity structure both within the cavity and outside the ice front (see section 3.4). We expect that subglacial runoff at the grounding line enhances basal melting of the ice tongue according to both theory (e.g., Jenkins, 2011) and observations, including recent mooring records from Petermann Gletscher in northern Greenland (Washam et al., 2019). Schaffer et al. (2020) find that the glacier freshwater flux (i.e., subglacial runoff together with basal melt) contributes 1.4% to the time-averaged cavity overturning strength. Their theoretical prediction of overturning strength based on density gradients across the sill

outside the pinned front agrees with their observational transport estimate throughout most of the year, but underestimates the overturning during May, June, and July. This is the period over which export at the PF site increases toward its summer maximum (Figure 7b). Thus, we infer that the freshwater flux constitutes a larger fraction of the overturning strength during the summer months, when subglacial runoff is present, relative to the annual mean.

Schaffer et al. (2020) find that 45% of outflow is directed through Dijmphna Sund, with the rest of the export through the pinned front, primarily through two gateways to the north of the PF mooring. While the prevailing flow direction at the ITM site at 150 m is inferred to be toward the pinned front (Figure 1a), currents are sometimes directed toward Dijmphna Sund, notably at 150 m during the cold pulse in January 2017, as well as intermittently throughout the year at the mid-depths as discussed in section 3.2. This suggests that the proportion of outflow through the various gateways could vary on time scales of days to weeks. Additionally, there is likely seasonal variability due to the subglacial runoff forcing, with the gateway closest to the PF site potentially accounting for a larger proportion of the export during summer.

The October 2016 shift in circulation from the overturning mode to the barotropic inflow mode (Figure 5c) is not preceded by any change in properties or currents observed at the PF site, suggesting that it is driven by a mechanism internal to the glacier-cavity system. The inflowing currents at all depths must be compensated by outflow at another location (assuming current direction does not reverse below 500 m or at another depth not captured by the current meters), possibly indicating a transition from the vertically sheared mean exchange flow to a primarily horizontally sheared exchange. Cross-fjord variation in exchange flow with horizontal shear is likely a persistent feature in the 79NG cavity due to its large width relative to the deformation radius, but it could be enhanced by factors such as a change in stratification or frictional influence, as observed in some estuarine systems (Lerczak et al., 2006; Valle-Levinson, 2008). The potential role of stratification in setting the exchange flow structure offers an additional mechanism by which runoff seasonality could drive shifts in circulation. However, this framework does not offer a straightforward explanation for later changes in the velocity profile observed at the ITM.

4.3. Ice Tongue Stability

Our estimates of residence time are broadly in agreement with other studies suggesting that renewal of ocean water in the 79NG cavity occurs within 1 year, and likely faster, with lower bounds of approximately 4 to 6 months (Schaffer et al., 2020; Wilson & Straneo, 2015). If the renewal time scale is sufficiently fast, ice tongue melt is predicted to increase proportionally to the square of a sustained temperature change (Holland, 2017; Holland, Jenkins, et al., 2008). The time scale of deep AIW warming inside the 79NG cavity observed in the ITM record, beginning in December 2016 and apparently sustained through July 2018, is likely longer than the residence time of the cavity and could thus be expected to accelerate thinning in the vicinity of the grounding line, which is presumably ongoing (Mouginot et al., 2015). Furthermore, the warming in November 2016 suggests an efficient mechanism for the shallow waters inside the cavity to adjust to changes on the shelf within weeks, causing a 33 $\pm$ 20% increase in estimated mean melt rate locally (Figure 8b). This could cause thinning in the vicinity of the ice front, where the ice draft is above the sill depth. The thinner ice is more vulnerable to rifting, which could ultimately result in significant calving, as observed at Petermann Gletscher (Münchow et al., 2014), though historical observations and modeling studies indicate that the bathymetric pinning points at the mouth of the 79NG cavity have a strong stabilizing influence on the ice tongue (Choi et al., 2017; Mouginot et al., 2015).

An improved mechanistic understanding of subannual variability will improve our understanding of the recent past and long-term fate of 79NG ice tongue. The ice tongue appears to have begun to thin in the early 2000s (Mouginot et al., 2015), coinciding roughly with summer breakups of previously quasipermanent landfast sea ice on the continental shelf (Sneed & Hamilton, 2016). Warming air temperatures drove increased surface melt of the ice sheet at around the same time (Khan et al., 2014; MacFerrin et al., 2019; Mouginot et al., 2019; Noël et al., 2018), likely causing subglacial runoff to increase (Slater et al., 2019). AIW has also warmed during that period (Figure 2a; Mayer et al., 2018). Each of these changes has seasonal or subannual analogues that can provide insight into changes in the 79NG cavity in the early 2000s, the ocean's role in the ice tongue thinning, and how these are likely to change in the future.

Changes in ice tongue thickness affect the ice tongue's buttressing of NEGIS, which holds a 1.1 m sea level equivalent (Morlighem et al., 2014). New studies indicate that the ocean around northeast Greenland is likely to experience the most dramatic warming of any Greenland region through 2100 (Slater et al., 2019)

and suggest that ocean warming may have driven major retreat of the 79NG grounding line relative to its present position during the Last Glacial Period (specifically 41–26 ka Tabone et al., 2019). An extended observational timeseries over multiple seasonal cycles would significantly improve our ability to distinguish between the various drivers of variability discussed here. The interpretation of these records would be further aided by additional measurements in other regions of the ice tongue and improved mapping of the bathymetry in and around the 79NG cavity.

5. Conclusion

We present the first moored record of ocean circulation and property variability in the 79NG cavity. The deep cavity is filled with warm AIW year-round, and the upper water column is primarily filled with colder, fresher glacially modified water, including runoff-modified water during the summer and early fall. We find that subannual variability in AIW temperature inside the cavity is smaller than interannual variability and conclude that waters in the 79NG cavity have warmed since 1998.

We observe a mean along-fjord overturning circulation, with inflow of warm AIW at depth and export of glacially modified water near the ice tongue base. Shallow currents are highly variable on 3–10 day time scales, and the influence of tidal currents is minor. A secondary mode of along-fjord circulation is characterized by strong inflow and outflow at the mid-depths lasting weeks to months during late fall and early winter 2016. Currents are intermittently directed toward Dijmphna Sund to the north, especially in the mid-depths.

Warming and thickening of the AIW layer observed on the continental shelf in late fall 2016 cause warming observed at the shallow depth and mid-depth at the ITM within 1 day, suggesting a wave-like mechanism for rapid propagation of ocean property variability into the cavity. Advection of warmer AIW at the ITM site is observed first at 500 m in late December 2016, resulting in warming of 0.4°C through mid-July 2017. Thickening of the AIW within the cavity is observed during spring 2017. Subglacial runoff discharged at the grounding line is inferred to drive variability in ocean properties inside the cavity in fall 2016 and summer 2017, as well as circulation variability observed at the PF mooring in summer 2017.

Our results suggest that ocean properties in the 79NG cavity are closely linked to variability on the continental shelf, with changes in stratification and water mass properties propagating into the cavity on time scales of days to months and a renewal time scale of under 1 year. Therefore, we expect basal melt of the 79NG ice tongue to be sensitive to ocean variability driven by large-scale and continental shelf processes (Münchow et al., 2020; Schaffer et al., 2020). This is consistent with the inferred link between observed ice tongue thinning and ocean warming (Mayer et al., 2018), suggesting that ocean property variability is crucial to interannual variability and long-term thinning of the 79NG ice tongue.

Appendix A: Calculation of the Standard Error of the Mean for an Autocorrelated Time Series

The standard error of the mean $\bar{\sigma}$ is calculated as

$$\bar{\sigma} = \frac{\sigma}{\sqrt{N_{\text{eff}}}}, \tag{A1}$$

where σ is the standard deviation and N_{eff} is the number of degrees of freedom of the sample. For an autocorrelated time series, N_{eff}, also known as the equivalent sample size, is fewer than the total number of observations N. Following von Storch and Zwiers (1999), we calculate a decorrelation time scale τ_D for each of the observed time series as

$$\tau_D = \max\left(1 + 2\sum_{k=1}^{n-1}\left(1 - \frac{k}{n}\right)\rho(k), n\right), \tag{A2}$$

where $n = 2, \ldots, N$ and k is the lag of the autocorrelation function $\rho(k)$. The equivalent sample size used in Equation A1 is thus calculated as

$$N_{\text{eff}} = \frac{N}{\tau_D}. \tag{A3}$$

Data Availability Statement

All data are publicly available and can be obtained via the references cited in the text.

Acknowledgments
We would like to thank Jeff Pietro and John Kemp's team at WHOI for training N. J. W. in Ice-Tethered Mooring (ITM) deployment. We acknowledge the contributions of crew and technicians aboard R/V *Polarstern*. Donald Slater provided the timeseries of surface runoff from RACMO and the code for the melt parameterization and plume model. Jamie Holte assisted with data processing and archiving. We also thank Tore Hattermann, Isabela Le Bras, Bobby Sanchez, Jamie Holte, and Momme Hell for helpful discussions and suggestions. We are grateful to the two anonymous reviewers who helped to improve this manuscript through their thoughtful and thorough feedback. Funding for the ITM was provided by the Grossman Family Foundation through the WHOI Development Office. M. R. L. is supported by a National Defense Science and Engineering Graduate Fellowship. N. L. B. is supported by a grant from the National Science Foundation (NSF OCE-1536856).

References

AWI (2017). Polar research and supply vessel POLARSTERN operated by the Alfred-Wegener-Institute. *Journal of Large-Scale Research Facilities*, *3*, A119. https://doi.org/10.17815/jlsrf-3-163

Adusumilli, S., Fricker, H. A., Siegfried, M. R., Padman, L., Paolo, F. S., & Ligtenberg, S. R. M. (2018). Variable basal melt rates of Antarctic Peninsula ice shelves, 1994–2016. *Geophysical Research Letters*, *45*, 4086–4095. https://doi.org/10.1002/2017GL076652

Arzeno, I. B., Beardsley, R. C., Limeburner, R., Owens, B., Padman, L., Springer, S. R., et al. (2014). Ocean variability contributing to basal melt rate near the ice front of Ross Ice Shelf, Antarctica. *Journal of Geophysical Research: Oceans*, *119*, 4214–4233. https://doi.org/10.1002/2014JC009792

Bell, R. E., Chu, W., Kingslake, J., Das, I., Tedesco, M., Tinto, K. J., et al. (2017). Antarctic ice shelf potentially stabilized by export of meltwater in surface river. *Nature*, *544*(7650), 344–348. https://doi.org/10.1038/nature22048

Beszczynska-Möller, A., Fahrbach, E., Schauer, U., & Hansen, E. (2012). Variability in Atlantic water temperature and transport at the entrance to the Arctic Ocean, 1997–2010. *ICES Journal of Marine Science*, *69*(5), 852–863. https://doi.org/10.1093/icesjms/fss056

Bjørk, A. A., Kruse, L. M., & Michaelsen, P. B. (2015). Brief communication: Getting Greenland's glaciers right—A new data set of all official Greenlandic glacier names. *The Cryosphere*, *9*(6), 2215–2218. https://doi.org/10.5194/tc-9-2215-2015

Chelton, D. B., DeSzoeke, R. A., Schlax, M. G., El Naggar, K., & Siwertz, N. (1998). Geographical variability of the first baroclinic Rossby radius of deformation. *Journal of Physical Oceanography*, *28*, 433–460.

Choi, Y., Morlighem, M., Rignot, E., Mouginot, J., & Wood, M. (2017). Modeling the response of Nioghalvfjerdsfjorden and Zachariae Isstrøm glaciers, Greenland, to ocean forcing over the next century. *Geophysical Research Letters*, *44*, 11,071–11,079. https://doi.org/10.1002/2017GL075174

Chu, V. W. (2014). Greenland ice sheet hydrology: A review. *Progress in Physical Geography: Earth and Environment*, *38*(1), 19–54. https://doi.org/10.1177/0309133313507075

Davis, P. E. D., Jenkins, A., Nicholls, K. W., Brennan, P. V., Abrahamsen, E. P., Heywood, K. J., et al. (2018). Variability in basal melting beneath Pine Island Ice Shelf on weekly to monthly timescales. *Journal of Geophysical Research: Oceans*, *123*, 8655–8669. https://doi.org/10.1029/2018JC014464

de Steur, L., Hansen, E., Mauritzen, C., Beszczynska-Möller, A., & Fahrbach, E. (2014). Impact of recirculation on the East Greenland Current in Fram Strait: Results from moored current meter measurements between 1997 and 2009. *Deep-Sea Research Part I*, *92*(March 2018), 26–40. https://doi.org/10.1016/j.dsr.2014.05.018

Dupont, T. K., & Alley, R. B. (2005). Assessment of the importance of ice-shelf buttressing to ice-sheet flow. *Geophysical Research Letters*, *32*, L05403. https://doi.org/10.1029/2004GL022024

Gade, H. G. (1979). Melting of ice in sea water: A primitive model with application to the Antarctic ice shelf and icebergs. *Journal of Physical Oceanography*, *9*(1), 189–198. https://doi.org/10.1175/1520-0485(1979)009<0189:MOIISW>2.0.CO;2

Hattermann, T., Isachsen, P. E., von Appen, W.-J., Albretsen, J., & Sundfjord, A. (2016). Eddy-driven recirculation of Atlantic Water in Fram Strait. *Geophysical Research Letters*, *43*, 3406–3414. https://doi.org/10.1002/2016GL068323

Hattermann, T., Nst, O. A., Lilly, J. M., & Smedsrud, L. H. (2012). Two years of oceanic observations below the Fimbul Ice Shelf, Antarctica. *Geophysical Research Letters*, *39*, L12605. https://doi.org/10.1029/2012GL051012

Hill, E. A., Carr, J. R., Stokes, C. R., & Gudmundsson, G. H. (2018). Dynamic changes in outlet glaciers in northern Greenland from 1948 to 2015. *The Cryosphere*, *12*(10), 3243–3263. https://doi.org/10.5194/tc-12-3243-2018

Holland, P. R. (2017). The transient response of ice shelf melting to ocean change. *Journal of Physical Oceanography*, *47*(8), 2101–2114.

Holland, P. R., Jenkins, A., & Holland, D. M. (2008). The response of ice shelf basal melting to variations in ocean temperature. *Journal of Climate*, *21*(11), 2558–2572. https://doi.org/10.1175/2007JCLI1909.1

Holland, D. M., Thomas, R. H., de Young, B., Ribergaard, M. H., & Lyberth, B. (2008). Acceleration of Jakobshavn Isbræ triggered by warm subsurface ocean waters. *Nature Geoscience*, *1*(10), 659–664. https://doi.org/10.1038/ngeo316

Jackson, R. H., Straneo, F., & Sutherland, D. A. (2014). Externally forced fluctuations in ocean temperature at Greenland glaciers in non-summer months. *Nature Geoscience*, *7*(7), 503–508.

Jenkins, A. (2011). Convection-driven melting near the grounding lines of ice shelves and tidewater glaciers. *Journal of Physical Oceanography*, *41*(12), 2279–2294. https://doi.org/10.1175/JPO-D-11-03.1

Jenkins, A., Nicholls, K. W., & Corr, H. F. J. (2010). Observation and parameterization of ablation at the base of Ronne Ice Shelf, Antarctica. *Journal of Physical Oceanography*, *40*(10), 2298–2312. https://doi.org/10.1175/2010JPO4317.1

Johnson, H. L., Münchow, A., Falkner, K. K., & Melling, H. (2011). Ocean circulation and properties in Petermann Fjord, Greenland. *Journal of Geophysical Research*, *116*, C01003. https://doi.org/10.1029/2010JC006519

Jordan, J. R., Holland, P. R., Jenkins, A., Piggott, M. D., & Kimura, S. (2014). Modeling ice-ocean interaction in ice-shelf crevasses. *Journal of Geophysical Research: Oceans*, *119*, 995–1008. https://doi.org/10.1002/2013JC009208

Joughin, I., Smith, B. E., Shean, D. E., & Floricioiu, D. (2014). Brief Communication: Further summer speedup of Jakobshavn Isbræ. *The Cryosphere*, *8*(1), 209–214. https://doi.org/10.5194/tc-8-209-2014

Khan, S. A., Kjær, K. H., Bevis, M., Bamber, J. L., Wahr, J., Kjeldsen, K. K., et al. (2014). Sustained mass loss of the northeast Greenland ice sheet triggered by regional warming. *Nature Climate Change*, *4*, 292–299. https://doi.org/10.1038/nclimate2161

Langley, K., Kohler, J., Sinisalo, A., Øyan, M. J., Hamran, S. E., Hattermann, T., et al. (2014). Low melt rates with seasonal variability at the base of Fimbul Ice Shelf, East Antarctica, revealed by in situ interferometric radar measurements. *Geophysical Research Letters*, *41*, 8138–8146. https://doi.org/10.1002/2014GL061782

Lerczak, J. A., Geyer, W. R., & Chant, R. J. (2006). Mechanisms driving the time-dependent salt flux in a partially stratified estuary. *Journal of Physical Oceanography*, *36*(12), 2296–2311. https://doi.org/10.1175/JPO2959.1

MacFerrin, M., Machguth, H., van As, D., Charalampidis, C., Stevens, C. M., Heilig, A., et al. (2019). Rapid expansion of Greenland's low-permeability ice slabs. *Nature*, *573*(7774), 403–407. https://doi.org/10.1038/s41586-019-1550-3

Marnela, M., Rudels, B., Houssais, M.-N., Beszczynska-Möller, A., & Eriksson, P. B. (2013). Recirculation in the Fram Strait and transports of water in and north of the Fram Strait derived from CTD data. *Ocean Science*, *9*(3), 499–519. https://doi.org/10.5194/os-9-499-2013

Mayer, C., Reeh, N., Jung-Rothenhäusler, F., Huybrechts, P., & Oerter, H. (2000). The subglacial cavity and implied dynamics under Nioghalvfjerdsfjorden Glacier, NE-Greenland. *Geophysical Research Letters*, *27*(15), 2289–2292. https://doi.org/10.1029/2000GL011514

Mayer, C., Schaffer, J., Hattermann, T., Floricioiu, D., Krieger, L., Dodd, P. A., et al. (2018). Large ice loss variability at Nioghalvfjerdsfjorden Glacier, Northeast-Greenland. *Nature Communications*, *9*(1), 2768. https://doi.org/10.1038/s41467-018-05180-x

McDougall, T. J., & Barker, P. M. (2011). Getting started with TEOS-10 and the Gibbs Seawater (GSW) Oceanographic Toolbox.

Millgate, T., Holland, P. R., Jenkins, A., & Johnson, H. L. (2013). The effect of basal channels on oceanic ice-shelf melting. *Journal of Geophysical Research: Oceans*, *118*, 6951–6964. https://doi.org/10.1002/2013JC009402

Morlighem, M., Rignot, E., Mouginot, J., Seroussi, H., & Larour, E. (2014). Deeply incised submarine glacial valleys beneath the Greenland ice sheet. *Nature Geoscience*, *7*(6), 418–422. https://doi.org/10.1038/ngeo2167

Morlighem, M., Williams, C. N., Rignot, E., An, L., Arndt, J. E., Bamber, J. L., et al. (2017a). BedMachine v3: Complete bed topography and ocean bathymetry mapping of Greenland from multibeam echo sounding combined with mass conservation. *Geophysical Research Letters*, *44*, 11,051–11,061. https://doi.org/10.1002/2017GL074954

Morlighem, M., Williams, C. N., Rignot, E., An, L., Arndt, J. E., Bamber, J. L., et al. (2017b). *IceBridge BedMachine Greenland, Version 3*. Boulder, Colorado, USA: NASA National Snow and Ice Data Center Distributed Active Archive Center. https://doi.org/10.5067/2CIX82HUV88Y

Motyka, R. J., Truffer, M., Fahnestock, M., Mortensen, J., Rysgaard, S., & Howat, I. (2011). Submarine melting of the 1985 Jakobshavn Isbræ floating tongue and the triggering of the current retreat. *Journal of Geophysical Research*, *116*, F01007. https://doi.org/10.1029/2009JF001632

Mouginot, J., Rignot, E., Bjørk, A. A., van den Broeke, M., Millan, R., Morlighem, M., et al. (2019). Forty-six years of Greenland Ice Sheet mass balance from 1972 to 2018. *Proceedings of the National Academy of Sciences*, *116*(19), 9239 LP–9244. https://doi.org/10.1073/pnas.1904242116

Mouginot, J., Rignot, E., Scheuchl, B., Fenty, I., Khazendar, A., Morlighem, M., et al. (2015). Fast retreat of Zachariæ Isstrøm, northeast Greenland. *Science*, *350*(6266), 1357 LP–1361. https://doi.org/10.1126/science.aac7111

Münchow, A., Padman, L., & Fricker, H. A. (2014). Interannual changes of the floating ice shelf of Petermann Gletscher, North Greenland, from 2000 to 2012. *Journal of Glaciology*, *60*(221), 489–499. https://doi.org/10.3189/2014JoG13J135

Münchow, A., Schaffer, J., & Kanzow, T. (2020). Ocean circulation connecting Fram Strait to glaciers off northeast Greenland: Mean flows, topographic Rossby waves, and their forcing. *Journal of Physical Oceanography*, *50*(2), 509–530. https://doi.org/10.1175/JPO-D-19-0085.1

Noël, B., van de Berg, W. J., van Wessem, J. M., van Meijgaard, E., van As, D., Lenaerts, J. T. M., et al. (2018). Modelling the climate and surface mass balance of polar ice sheets using RACMO2—Part 1: Greenland (1958–2016). *The Cryosphere*, *12*(3), 811–831. https://doi.org/10.5194/tc-12-811-2018

Padman, L., Siegfried, M. R., & Fricker, H. A. (2018). Ocean tide influences on the Antarctic and Greenland ice sheets. *Reviews of Geophysics*, *56*, 142–184. https://doi.org/10.1002/2016RG000546

Pawlowicz, R., Beardsley, B., & Lentz, S. (2002). Classical tidal harmonic analysis including error estimates in MATLAB using T_TIDE. *Computers & Geosciences*, *28*(8), 929–937. https://doi.org/10.1016/S0098-3004(02)00013-4

Reeh, N., Thomsen, H. H., Higgins, A. K., & Weidick, A. (2001). Sea ice and the stability of north and northeast Greenland floating glaciers. *Annals of Glaciology*, *33*, 474–480. https://doi.org/10.3189/172756401781818554

Schaffer, J., Kanzow, T., von Appen, W.-J., von Albedyll, L., Arndt, J. E., & Roberts, D. H. (2020). Bathymetry constrains ocean heat supply to Greenland's largest glacier tongue. *Nature Geoscience*, *13*(3), 227–231. https://doi.org/10.1038/s41561-019-0529-x

Schaffer, J., & Mayer, C. (2018). Physical oceanography during NE-Greenland expeditions 1997/98. PANGAEA https://doi.org/10.1594/PANGAEA.891386

Schaffer, J., von Appen, W. J., Dodd, P. A., Hofstede, C., Mayer, C., de Steur, L., & Kanzow, T. (2017). Warm water pathways toward Nioghalvfjerdsfjorden Glacier, Northeast Greenland. *Journal of Geophysical Research: Oceans*, *122*, 4004–4020. https://doi.org/10.1002/2016JC012462

Schaffer, J., von Appen, W.-J., & Kanzow, T. (2019). Physical oceanography and current meter data from mooring 79N1-1 at the continental shelf off Northeast Greenland. PANGAEA. https://doi.org/10.1594/PANGAEA.909452

Slater, D. A., Nienow, P. W., Goldberg, D. N., Cowton, T. R., & Sole, A. J. (2017). A model for tidewater glacier undercutting by submarine melting. *Geophysical Research Letters*, *44*, 2360–2368. https://doi.org/10.1002/2016GL072374

Slater, D. A., Straneo, F., Felikson, D., Little, C. M., Goelzer, H., Fettweis, X., & Holte, J. (2019). Estimating Greenland tidewater glacier retreat driven by submarine melting. *The Cryosphere*, *13*(9), 2489–2509. https://doi.org/10.5194/tc-13-2489-2019

Sneed, W. A., & Hamilton, G. S. (2016). Recent changes in the Norske Oer Ice Barrier, coastal Northeast Greenland. *Annals of Glaciology*, *57*(73), 47–55. https://doi.org/10.1017/aog.2016.21

Stanton, T. P., Shaw, W. J., Truffer, M., Corr, H. F. J., Peters, L. E., Riverman, K. L., et al. (2013). Channelized ice melting in the ocean boundary layer beneath Pine Island Glacier, Antarctica. *Science*, *341*(6151), 1236–1239. https://doi.org/10.1126/science.1239373

Stevens, C., Hulbe, C., Brewer, M., Stewart, C., Robinson, N., Ohneiser, C., & Jendersie, S. (2020). Ocean mixing and heat transport processes observed under the Ross Ice Shelf control its basal melting. *Proceedings of the National Academy of Sciences*, *117*(29), 16,799–16,804. https://doi.org/10.1073/pnas.1910760117

Stewart, C. L., Christoffersen, P., Nicholls, K. W., Williams, M. J. M., & Dowdeswell, J. A. (2019). Basal melting of Ross Ice Shelf from solar heat absorption in an ice-front polynya. *Nature Geoscience*, *12*(6), 435–440. https://doi.org/10.1038/s41561-019-0356-0

Straneo, F. (2020). Water temperature and salinity taken by CTD and XBT from vessel Arctic Sunrise in Kangerdlugssuaq Fjord and Nioghalvfjerdsfjorden, Greenland, from 2009-08-28 to 2009-09-08 (NCEI Accession 0210954). NOAA National Centers for Environmental Information https://accession.nodc.noaa.gov/0210954

Straneo, F., & Cenedese, C. (2015). The dynamics of Greenland's glacial fjords and their role in climate. *Annual Review of Marine Science*, *7*(1), 89–112. https://doi.org/10.1146/annurev-marine-010213-135133

Straneo, F., Hamilton, G. S., Sutherland, D. A., Stearns, L. A., Davidson, F., Hammill, M. O., et al. (2010). Rapid circulation of warm subtropical waters in a major glacial fjord in East Greenland. *Nature Geoscience*, *3*(3), 182–186. https://doi.org/10.1038/ngeo764

Straneo, F., & Wilson, N. (2020). Water temperature and salinity taken by expandable CTD from ice edge in Nioghalvfjerdsfjorden, Northeast Greenland, on 2016-08-23 (NCEI Accession 0210955). NOAA National Centers for Environmental Information https://accession.nodc.noaa.gov/0210955

Tabone, I., Robinson, A., Alvarez-Solas, J., & Montoya, M. (2019). Submarine melt as a potential trigger of the North East Greenland Ice Stream margin retreat during Marine Isotope Stage 3. *The Cryosphere*, *13*(7), 1911–1923. https://doi.org/10.5194/tc-13-1911-2019

Toole, J. M., Krishfield, R., & Woods Hole Oceanographic Institution Ice-Tethered Profiler Program (2016). Oceanographic profile observations collected from station ITM-5 by Woods Hole Oceanographic Institution (WHOI) in the 79 North Glacier, Greenland, from 2016-08-23 to 2018-12-22 (NCEI Accession 0157557). NOAA National Centers for Environmental Information https://accession.nodc.noaa.gov/0157557

Valle-Levinson, A. (2008). Density-driven exchange flow in terms of the Kelvin and Ekman numbers. *Journal of Geophysical Research*, *113*, C04001. https://doi.org/10.1029/2007JC004144

von Storch, H., & Zwiers, F. W. (1999). Specific statistical concepts in climate research. In F. W. Zwiers, & H. von Storch (Eds.), *Statistical analysis in climate research* (pp. 371–390). Cambridge: Cambridge University Press.

Washam, P., Münchow, A., & Nicholls, K. W. (2018). A decade of ocean changes impacting the ice shelf of Petermann Gletscher , Greenland. *Journal of Physical Oceanography*, *48*, 2477–2493.

Washam, P., Nicholls, K. W., Münchow, A., & Padman, L. (2019). Summer surface melt thins Petermann Gletscher Ice Shelf by enhancing channelized basal melt. *Journal of Glaciology*, *65*(252), 662–674.

Wilson, N. J., & Straneo, F. (2015). Water exchange between the continental shelf and the cavity beneath Nioghalvfjerdsbræ (79 North Glacier). *Geophysical Research Letters*, *42*, 7648–7654. https://doi.org/10.1002/2015GL064944

Wilson, N. J., Straneo, F., & Heimbach, P. (2017). Satellite-derived submarine melt rates and mass balance (2011-2015) for Greenland's largest remaining ice tongues. *Cryosphere*, *11*(6), 2773–2782. https://doi.org/10.5194/tc-11-2773-2017

Zhao, K. X., Stewart, A. L., & McWilliams, J. C. (2019). Sill-influenced exchange flows in ice shelf cavities. *Journal of Physical Oceanography*, *49*(1), 163–191. https://doi.org/10.1175/JPO-D-18-0076.1